Article

Quantum-enabled millimetre wave to optical transduction using neutral atoms

Aishwarya Kumar[1,2,4 ✉], Aziza Suleymanzade[1,4], Mark Stone[1,4], Lavanya Taneja[1], Alexander Anferov[1], David I. Schuster[1,3] & Jonathan Simon[1,2,3]

Early experiments with transiting circular Rydberg atoms in a superconducting resonator laid the foundations of modern cavity and circuit quantum electrodynamics[1], and helped explore the defining features of quantum mechanics such as entanglement. Whereas ultracold atoms and superconducting circuits have since taken rather independent paths in the exploration of new physics, taking advantage of their complementary strengths in an integrated system enables access to fundamentally new parameter regimes and device capabilities[2,3]. Here we report on such a system, coupling an ensemble of cold ^{85}Rb atoms simultaneously to an, as far as we are aware, first-of-its-kind optically accessible, three-dimensional superconducting resonator[4] and a vibration-suppressed optical cavity in a cryogenic (5 K) environment. To demonstrate the capabilities of this platform, and with an eye towards quantum networking[5], we leverage the strong coupling between Rydberg atoms and the superconducting resonator to implement a quantum-enabled millimetre wave (mmwave) photon to optical photon transducer[6]. We measured an internal conversion efficiency of 58(11)%, a conversion bandwidth of 360(20) kHz and added thermal noise of 0.6 photons, in agreement with a parameter-free theory. Extensions of this technique will allow near-unity efficiency transduction in both the mmwave and microwave regimes. More broadly, our results open a new field of hybrid mmwave/optical quantum science, with prospects for operation deep in the strong coupling regime for efficient generation of metrologically or computationally useful entangled states[7] and quantum simulation/computation with strong non-local interactions[8].

Superconducting circuits, cold atoms and optical photons form the basis of much of modern quantum science and many quantum technologies[9], having driven significant progress in quantum information and metrology, and have led to deep insights into the nature of strongly correlated matter. Nonetheless, these platforms have varied strengths, rendering each suitable for distinct applications. To combine these diverse strengths, a long-standing objective is the development of hybrid platforms that efficiently transduce individual microwave photons—the natural excitations of superconducting/solid-state quantum processors[10]—to optical photons.

Conversion of quantum information from stationary computation qubits to flying optical qubits lies at the heart of quantum networking tasks, from linking remote quantum computers for scaling to fault tolerance, to quantum key distribution[11] and secondary technologies such as quantum repeaters[12]. In general, it is desirable for the transducer to (1) be efficient—the loss of information through various decay channels during the conversion process should be minimal; (2) have a high bandwidth—the conversion should be much faster than the decay of the stationary qubits to preserve coherence; and (3) be noiseless—the added

noise, typically thermal, should be much smaller than one photon to preserve the integrity of the quantum information[13]. Indeed, because the microwave backgrounds are so large at room temperature, the transduction process must take place at the base of a low-temperature cryostat, with only the optical photons bridging the gap between room temperature and cryogenic environments.

There has been tremendous progress towards building such systems for superconducting qubits in recent years, particularly by using materials with direct electro-optic coupling[14–16] or some combination of piezo-electric, electromechanical and optomechanical couplings[17–21]: The state of a superconducting qubit was transduced to the optical domain through a nanomechanical resonator[20]; the added noise was low but the internal conversion efficiency was limited to 10^{-3}. A silicon nitride membrane simultaneously coupled to an LC resonator and an optical cavity was employed to efficiently read out a qubit state, but with significant noise and limited bandwidth[19]. Broadly, these approaches are limited by material absorption of the strong microwave and optical pumps required not only to bridge the microwave-to-optical energy gap, but also to achieve the strong couplings necessary for efficient transduction[18,22].

[1]The Department of Physics, The James Franck Institute and The Pritzker School of Molecular Engineering, The University of Chicago, Chicago, IL, USA. [2]The Department of Physics, Stanford University, Stanford, CA, USA. [3]The Department of Applied Physics, Stanford University, Stanford, CA, USA. [4]These authors contributed equally: Aishwarya Kumar, Aziza Suleymanzade, Mark Stone. ✉e-mail: ashk.phy@gmail.com
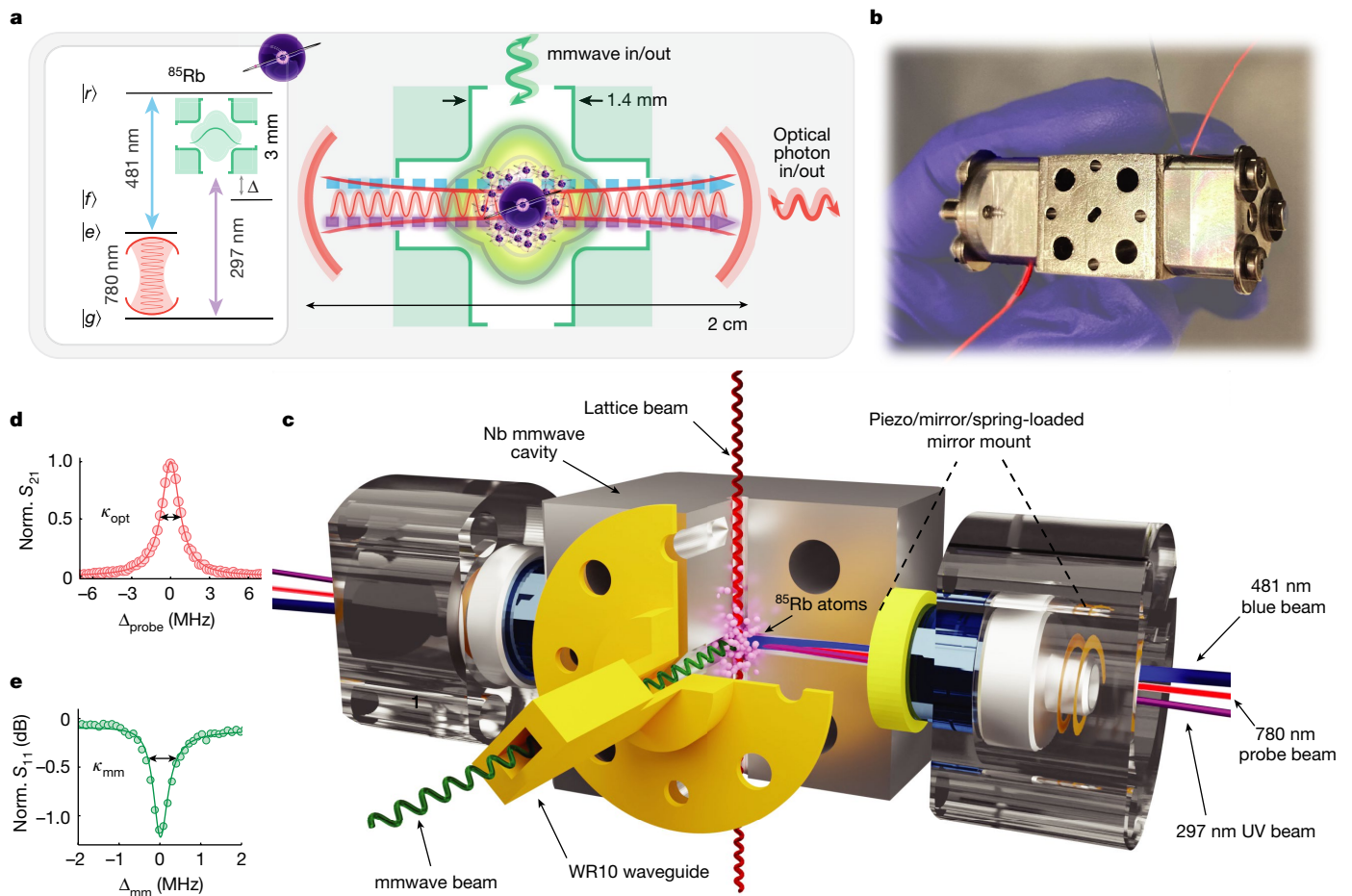
Fig. 1 | Experimental setup. a, Schematic of the system. Left, atomic energy levels and wavelengths of light involved in transduction; right, internal structure of the optical and mmwave interface. The atoms are coupled simultaneously to an optical cavity (red) and a superconducting mmwave resonator (green). The interconversion loop is closed by the blue (481 nm) and UV (297 nm) control lasers. **b**, Image of the physical hybrid cavity. **c**, Expanded view of the main assembly. The mmwave mode is hosted at the intersection of three orthogonal cylindrical waveguides machined in a niobium spacer. One of the waveguides is used to transport cold ^{85}Rb atoms in a one-dimensional optical lattice (red vertical beam) from a magneto-optical trap 6.5 cm above

the structure. A second waveguide provides optical access for formation of the optical cavity by affixing mirrors and piezos at both ends of the spacer, using a spring-loaded design for vibrational stability (Supplementary Information A3). It also provides a path for the 481 nm and UV lasers (shown in blue and purple, respectively). The third waveguide allows us to probe the resonator with an external mmwave drive. **d**, Bare optical cavity transmission, normalized to peak value, with full-width, half-maximum (FWHM) linewidth $\kappa_{opt} = 2\pi \times 1.7$ MHz. The solid line is a Lorentzian fit. **e**, Reflection spectrum of the superconducting mmwave cavity at 5 K, normalized to a far off-resonant value, with FWHM linewidth $\kappa_{mm} = 2\pi \times 800$ kHz.

Neutral atoms offer a promising alternative[23–25]: in their ground states, atoms couple strongly to optical photons and, when excited to Rydberg states, couple strongly to microwave photons. Free-space interconversion with Rydberg atoms has been demonstrated at room temperature[26,27], but coupling the atoms to a high-quality-factor superconducting resonator at cryogenic temperatures is ultimately essential to enable transduction of a superconducting qubit with low thermal noise and high efficiency. In spite of seminal early experiments[1], combining those techniques with modern innovations in neutral atom control has remained elusive[28].

In this work we overcome these difficulties, strongly coupling cold, Rydberg-dressed atoms to a superconducting millimetre wave (mmwave) resonator crossed with an optical cavity, and employ this unique platform to interconvert optical and mmwave photons. These breakthroughs are enabled by a new three-dimensional mmwave resonator and a vibration-stabilized optical cavity in a tightly integrated design. Our mmwave resonator confines photons to a volume of approximately $\lambda^3/10$ while maintaining the optical access required to (1) form an optical cavity, (2) load and (3) optically address the atoms[4]. We individually characterize coupling of the atoms to fields involved

in the transduction process by probing the transmission of the optical cavity, enabling us to construct a simple parameter-free model of interconversion. To measure the performance of our transducer, we drive the mmwave resonator and observe the output of the optical cavity and find good agreement with the model. We then compare the output of the optical cavity with and without mmwave drives and cleanly separate the interconversion of thermal photons from that of an applied coherent drive, both in the optical photon count rates and second-order correlations, further confirming the ability to operate in the single-photon regime.

Our mmwave resonator traps photons at the intersection of three orthogonal cylindrical waveguides drilled in a solid cuboid of high-purity niobium while the waveguides themselves remain evanescent, preventing photon leakage[4] (Fig. 1b,d and Supplementary Information A2). We use one of the waveguides to make an optical cavity by mounting mirrors at both ends. The mirrors and piezos are clamped using spring washers to minimize the effect of cryofridge vibrations (Supplementary Information A3). A second waveguide is used to load an ensemble of atoms in the centre of the resonator using a one-dimensional optical transport lattice. All optical fields necessary
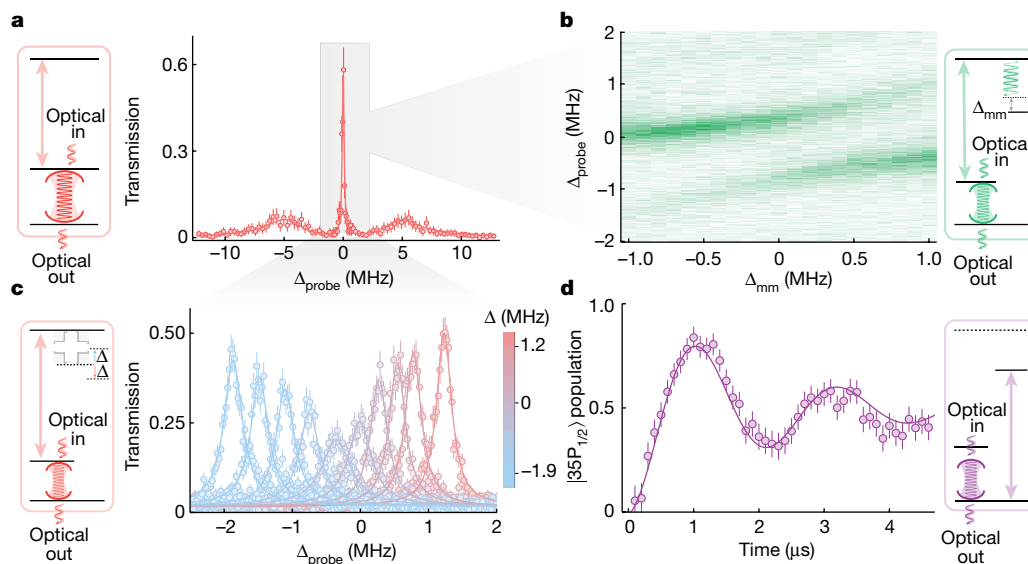
Fig. 2 | The building blocks for transduction. a–d, Each leg of the conversion loop can be independently characterized by probing the transmission of the optical cavity. **a,** A 780 nm photon couples an ensemble of atoms to a collective $5P_{3/2}$ state, which is further coupled by a blue (481 nm) photon to a collective $36S_{1/2}$ Rydberg state. We observe the excitations of this system in the transmission of the optical cavity as we scan the 780 nm probe laser across the cavity resonance (with detuning Δ_{probe}). The atoms hybridize with the optical mode to form two bright polaritons (whose large width comes from the lossy $5P_{3/2}$ state $\Gamma \approx 2\pi \times 6$ MHz) and a dark polariton (narrow central feature), which contains only an excitation into the Rydberg state for its atomic component. We typically operate on resonance with the dark polariton for transduction, to prevent efficiency loss due to decay of the $5P_{3/2}$ state. **b,** Application of a coherent mmwave drive near the atomic $36S_{1/2} \leftrightarrow 35P_{1/2}$ resonance, but detuned by $\Delta \approx 2\pi \times 12.4$ MHz from the mmwave cavity, splits the dark polariton peak due to admixing of the $36S_{1/2}$ and $35P_{1/2}$ Rydberg states by the mmwave drive.

Scanning the mmwave drive frequency (with detuning Δ_{mm}) produces an avoided crossing, enabling us to determine the $36S_{1/2} \leftrightarrow 35P_{1/2}$ resonance frequency and therefore the detuning between this transition and the mmwave cavity. **c,** To Stark-tune the atomic transition into resonance with the primary science mmwave cavity mode we use an auxiliary, tuning, mmwave mode that is detuned from the atomic transition by $2\pi \times 1.9$ GHz. At atomic resonance with the mmwave science mode, we observe a significant broadening and reduction in peak height of the dark polariton transmission feature due to coupling with the vacuum and thermal fields of the mmwave cavity. **d,** Population in the $5S_{1/2}$ state after UV laser pulses of variable length. In the absence of the 481 nm coupling beam and with the $36S_{1/2} \leftrightarrow 35P_{1/2}$ transition detuned from the mmwave cavity, we observe Rabi flopping which allows us to determine the UV Rabi frequency $\Omega_{uv} = 2\pi \times 230$ kHz. We measure the ground versus Rydberg atomic population via a dispersive shift of the optical cavity.

to address the atoms are routed through these two waveguides, with the Gaussian waists of the laser beams much smaller than the waveguide diameters. We use the third waveguide to couple in mmwave photons (Fig. 1d).

Our transduction scheme may be understood as four-wave mixing mediated by an atomic ensemble, as shown in Fig. 1a (Methods). In the limit of a large detuning ($|\Delta| \gg |\Omega_{uv}|$) between the mmwave cavity and the $36S_{1/2} \leftrightarrow 35P_{1/2}$ atomic transition, the linearized interaction Hamiltonian (Supplementary Information B) may be written as

$$\mathcal{H}_{int}/\hbar = \sqrt{N}g_{opt}aE^{\dagger} + \Omega_b ER^{\dagger} + g_{mm}\frac{\sqrt{N}\Omega_{uv}}{\Delta}b^{\dagger}R + \text{h. c.} \quad (1)$$

where $E^{\dagger}$ and $R^{\dagger}$ are the bosonized collective excitation operators to the $5P_{3/2}$ and the $36S_{1/2}$ state, respectively, from a reservoir of N atoms in the $5S_{1/2}$ ground state; g_{opt} and g_{mm} are the single-atom coupling strengths for the optical (a) and mmwave (b) modes; Ω_b and Ω_{uv} are the Rabi frequencies for the 481 nm and ultraviolet (UV) fields; and h. c. is the Hermitian conjugate.

We now characterize the steps of the interconversion process by performing experiments that take optical photons incrementally around the transduction loop. We first omit the UV drive and detune the atoms from the mmwave cavity ($|\Delta| \gg |g_{mm}|$), leaving only three-level atoms coupled to the optical cavity and 481 nm control field (Fig. 2a) in the canonical Rydberg electromagnetically induced transparency (EIT) configuration[29,30]. In this regime, the relevant optical excitations of the system are cavity polaritons[30], quasiparticles consisting of a superposition of atomic and photonic components. Transmission of the optical cavity shows a dark polariton residing between two bright polaritons

(Fig. 2a). For interconversion, we operate on the dark polariton resonance to minimize loss and required pump powers (Supplementary Information E). In the limit of a spectrally resolved dark polariton, the transduction process can be understood as a beam splitter between mmwave and dark polariton modes (Supplementary Information B6). Fitting spectra such as those shown in Fig. 2a to analytical models from non-Hermitian perturbation theory[31] enables extraction of the parameters central to building a quantitative model of interconversion: N, the atom number, Ω_b the 481 nm Rabi frequency and Γ_R, the collectively suppressed decoherence rate of the Rydberg state[32] (Methods and Extended Data Table 1).

Before introduction of the quantized mmwave cavity field, we study the impact of a classical mmwave field on dark polariton resonance. This field drives the $36S_{1/2}$ atomic component of the polariton to the $35P_{1/2}$ state, producing Autler–Townes splitting of the dark polariton. The resulting avoided crossing as a function of mmwave drive frequency facilitates extraction of atomic transition frequency (Fig. 2b) and thereby determination of the detuning (Δ) of the atoms from the mmwave cavity.

We next explore the coupling of the atoms to the mmwave cavity vacuum by varying the detuning between atoms and the (undriven) mmwave cavity. In practice, this is achieved through an ac-Stark shift of the atomic Rydberg levels by driving a far-off-resonant (from atoms) tuning mode of the mmwave cavity (Methods and Supplementary Information A2). We observe a significant broadening of the dark polariton when the atoms are resonant with the mmwave cavity (Fig. 2c). This Purcell-like broadening results from vacuum coupling of the polariton to the $35P_{1/2}$ Rydberg state, enhanced by the thermal population of the mmwave cavity. The observed broadening is consistent with our
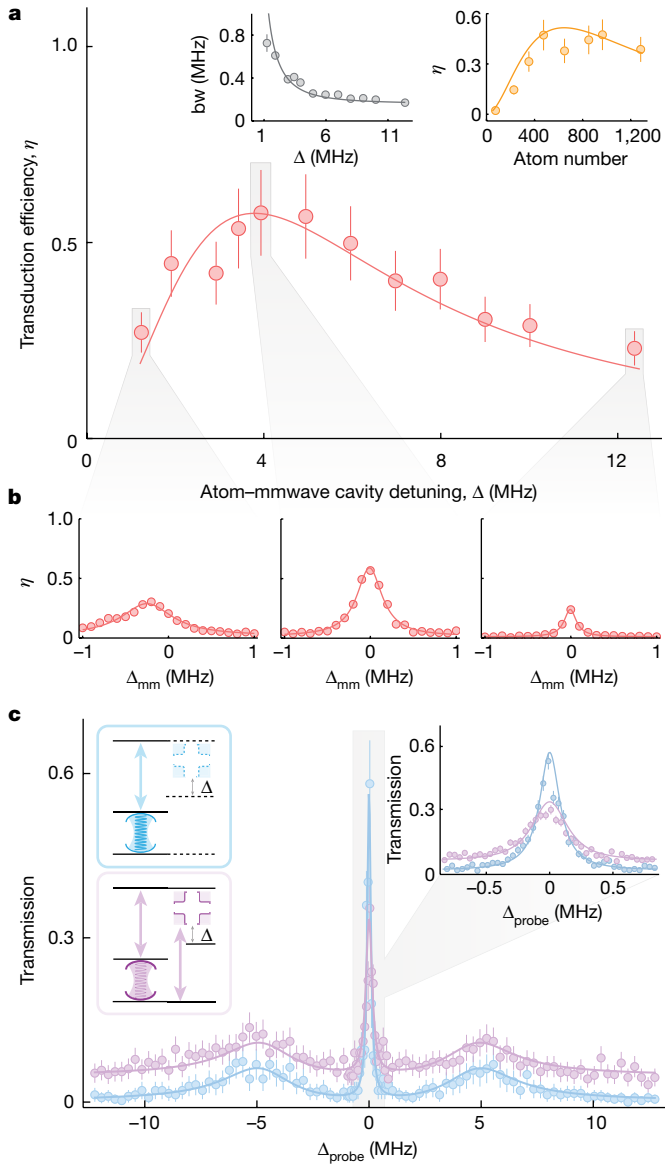
Fig. 3 | Transducer performance. a, Peak internal conversion efficiency (red) as atom–mmwave cavity detuning (Δ) is varied. Efficiency is maximized when the transduction process is impedance matched, which can also be controlled by varying the atom number, as in the right-hand inset (yellow), with $\Delta = 2\pi \times 3.9$ MHz fixed. **b**, For each point in **a** we scan mmwave drive frequency (detuning from cavity Δ_{mm}) through the science mode and fit the resulting spectrum to a Lorentzian with an offset to extract peak conversion efficiency. We also extract the interconversion bandwidth (bw, grey, left-hand inset in **a**) from the FWHM of the fitted Lorentzians. Here we operate with effective atom number $N \approx 600$. **c**, We indirectly probe optical-to-mmwave transduction by observing optical transmission with (purple) and without (blue) the 297 nm UV laser ($\Delta \approx 2\pi \times 4.2$ MHz and $N \approx 500$). The inset zooms into the dark polariton, which is suppressed and broadened by the additional loss of conversion to mmwave photons. The offset reflects conversion of thermal mmwave photons into optical photons. **a**–**c**, All solid curves are parameter-free theory except for the blue fit to the spectrum in **c**, which provides the parameters. For our system, it is always favourable to fix the 481 nm and UV powers to their maximum achievable values.

calculated value of $g_{mm} = 2\pi \times 182$ kHz and the expected thermal occupation $n_{th} \approx 0.6$ photons of a 100 GHz mode at 5 K (Methods).

The final ingredient required to close the interconversion loop is the direct UV (297 nm) transition between the ground state and the $35P_{1/2}$ state, which we explore separately rather than investigating its impact

on the dark polariton. We turn off the 481 nm beam, return to a large detuning between the mmwave cavity and the atoms and drive Rabi oscillations on $5S_{1/2} \leftrightarrow 35P_{1/2}$ with a variable-length UV pulse (Fig. 2d). The optical cavity is employed only to detect the transfer of atomic population via a dispersive shift of the cavity line[33]. This measurement directly calibrates Ω_{uv} (Methods and Extended Data Table 1), the final key parameter in Hamiltonian.

For the coupling scheme shown in Fig. 1a, with the Hamiltonian given by equation (1), the conversion efficiency is given by (Supplementary Information B)

$$\mathcal{E} = \frac{\kappa_{opt}^{ext} \kappa_{mm}^{ext}}{\kappa_{opt} \kappa_{mm}} \eta_{o \leftrightarrow mm} \qquad (2)$$

Here κ_{opt} and κ_{mm} are the total decay rates of the optical and mmwave cavities, respectively, and κ_{opt}^{ext} and κ_{mm}^{ext} are the associated outcoupling rates through their measurement ports.

We are now prepared to combine all of the couplings and perform transduction. We measure $\eta_{o \leftrightarrow mm}$, the internal conversion efficiency, by exciting the mmwave cavity with a classical drive of known average intracavity photon number, n_{ph}, and by measuring the converted photon count rate at an output port of the optical cavity (Methods). We typically operate at $n_{ph} \approx 2$.

To systematically study interconversion we first vary Δ, which controls C_{mm}, the collective cooperativity of the mmwave transition, through the steady-state dressing fraction in the $35P_{1/2}$ state (Methods). A clear maximum in the conversion efficiency can be seen near $\Delta \approx 2\pi \times 4$ MHz, where the transduction process is impedance matched (Fig. 3a). If we instead fix the detuning and vary the atom number (changing both the optical cooperativity, C_o, and C_{mm}), we observe a similar impedance matching in conversion efficiency variation (Fig. 3a, inset). For each efficiency measurement we also measure the interconversion bandwidth (Fig. 3a, inset, 3b), by directly probing $|S(\omega)|^2$, the transfer function of the interconverter (Supplementary Information B). We measure a peak efficiency of 58(11)% with a bandwidth 360(20) kHz, in agreement with our parameter-free theory (solid curves). Our measured mirror reflectivities and mmwave cavity outcoupling imply an end-to-end conversion efficiency of 2.5%, limited by the latter (Methods).

Due to the mmwave attenuators included to limit black-body heating of the mmwave cavity by the room temperature characterization setup (Extended Data Fig. 1), we cannot directly probe the reverse, optical-to-mmwave conversion process. Such attenuators will not be necessary in a quantum network, in which mmwave photons will be sourced from—and sent to—cryogenic quantum circuits. We instead observe this process indirectly through the loss of optical photons when measuring optical cavity transmission: We operate without an external mmwave drive and compare optical transmission with/without the UV beam, measuring a suppression and broadening of dark polariton resonance (Fig. 3c). The lost optical photons correspond not only to interconverted mmwave photons, but also to photons scattered into free space and reflected off the optical cavity due to impedance mismatch. We find that our measurement is in good agreement with our theory and the predicted conversion efficiency. Additionally, the optical cavity transmission in the presence of the UV beam experiences a probe frequency-independent background due to transduced thermal mmwave cavity photons.

To characterize this thermal noise, we operate the transducer near the nominally impedance matched point in Fig. 3a, vary the UV laser frequency to translate the transduction band in frequency and plot the observed optical count rate (Fig. 4a). Without an external mmwave drive, we observe a broad asymmetric feature that develops a narrow peak as a weak coherent drive ($n_{ph} = 0.55(5)$) is added. The narrow feature is a direct measurement of transduction bandwidth, with the wider feature reflecting thermal backgrounds emitted by the broad mmwave
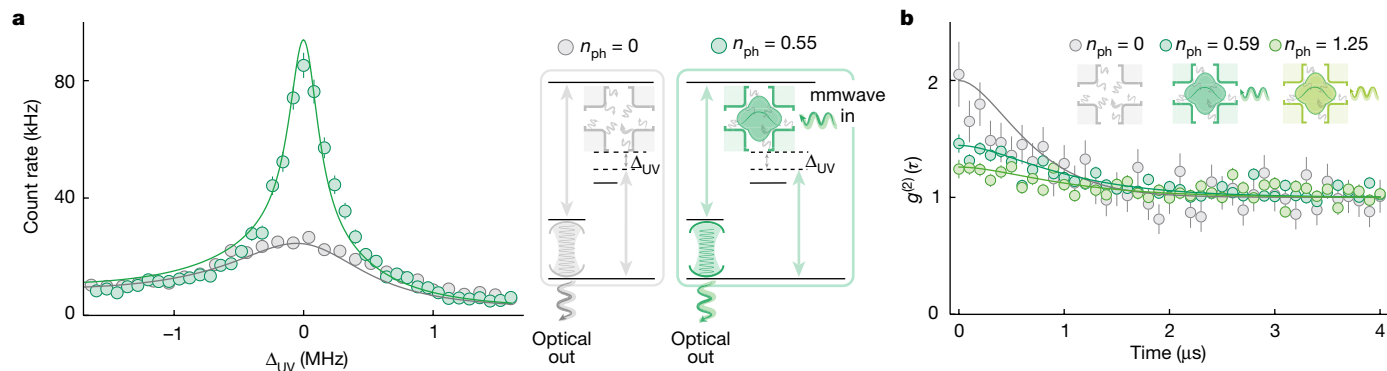
Fig. 4 | Thermal photons and intensity correlations. a, Count rate at the output of the optical cavity without an external mmwave drive (grey), and with a coherent mmwave drive with approximately 0.5 photons (green), as the frequency of the UV laser is scanned. The broad grey feature shows the interconversion of the broadband thermal drive of the mmwave cavity, and the conversion of a coherent drive quickly becomes lossy as the UV laser is tuned away from the dark polariton resonance. **b**, Measured second-order correlation functions of converted optical photons for various mmwave drive strengths: 0 drive photons (grey), 0.5 photons (dark green) and 1.1 photons (light green). **a,b**, Solid curves are theory with no free parameters. The statistical error in n_{ph} is about ±10%.

cavity. The asymmetry arises from variation in impedance matching as the UV is tuned towards the atomic resonance (lower Δ_{UV} in Fig. 4a). Because many of the thermal photons are outside the transduction band, the measured count rate for thermal photons is lower than it would be for a coherent drive with the same average photon number. The shape of the thermal feature, as well as peak count rates, match predictions from the Hamiltonian in equation (1) with the 0.6 thermal photons expected at 5 K (Methods). This implies that the input-referred added noise is simply 0.6 photons s^{-1} Hz^{-1}—the power spectral density of the input thermal drive at the frequency of the mmwave cavity.

To ensure that the observed noise photons are indeed thermal and not coherent backgrounds (for example, from the off-resonant tuning drive). we measure the second-order intensity correlation function of the converted optical photons $g^{(2)}(\tau)$ as we vary the external coherent mmwave drive strength (Fig. 4b). In the absence of the coherent drive, $g^{(2)}(0) \approx 2$ as expected for a thermal source. Once the coherently injected photon population exceeds the thermal population, $g^{(2)}(0)$ drops towards 1. Even for an entirely thermal input state, the decay time of $g^{(2)}(\tau)$ is set by the transduction bandwidth. The calculated $g^{(2)}(\tau)$ (Methods) for 0.6 thermal photons (a temperature of 5 K) agrees with the data.

We envision clear pathways to further improved transducer performance and coupling to superconducting qubits. The conversion efficiency is presently limited by the Rabi frequency of the 481 nm laser. Modifications to the mmwave mode and 481 nm/UV laser polarizations will significantly increase the 481 nm, UV and mmwave resonator coupling strengths and thereby push the efficiency to near unity (Methods). The added noise is presently set by the 5 K temperature of the mmwave cavity; cooling to 1 K would reduce this noise from 0.6 to under 0.01 photons and improve the mmwave cavity quality factor by more than 100-fold. Direct coupling between atoms and (around 10 GHz) transmon qubits is possible by working at higher principal quantum number atomic states in larger, colder resonators (Supplementary Information F). The introduction of a high-kinetic inductance resonator[34,35] as a mmwave-to-microwave link may obviate the need for direct microwave transitions in Rydberg atoms, thereby separating the sensitive microwave environment from the detrimental heating induced by the strong optical fields required for transduction.

These experiments demonstrate high-efficiency, wideband, quantum-enabled transduction between mmwave and optical photons, where added transducer noise is sufficiently low (below 1 photon) to preserve entanglement in the input field. Combined with superconducting qubits, they will comprise a complete quantum networking platform. More broadly, mmwave-to-optical conversion holds promise as an efficient means for detection of individual mmwave photons and may thus find applications in axion dark matter searches[36] and entanglement enhanced detection of mmwaves from astrophysical sources[37].

Beyond transduction, this work constitutes a powerful new route to non-local interactions between atoms enabled by the macroscopic physical extent of the mmwave resonator mode. Our platform can achieve single-particle cooperativities as high as $C \approx 6,000$ at temperatures of approximately 2 K (ref. [4]), thus enabling Heisenberg limited squeezing[7,38], and gates/couplings between non-adjacent atoms, as required for explorations of scrambling[8], and realizations of error correcting codes[39]. Indeed, the approach is even compatible with the optical access necessary for atom-arrays[40], for enabling a next generation of quantum computers combining Rydberg interaction-mediated nearest-neighbour gates and superconducting cavity-mediated long-range gates[41].

Online content

Any methods, additional references, Nature Portfolio reporting summaries, source data, extended data, supplementary information, acknowledgements, peer review information; details of author contributions and competing interests; and statements of data and code availability are available at https://doi.org/10.1038/s41586-023-05740-2.

1. Raimond, J. M., Brune, M. & Haroche, S. Manipulating quantum entanglement with atoms and photons in a cavity. *Rev. Mod. Phys.* **73**, 565–582 (2001).
2. Kurizki, G. et al. Quantum technologies with hybrid systems. *Proc. Natl Acad. Sci. USA* **112**, 3866–3873 (2015).
3. Clerk, A. A., Lehnert, K. W., Bertet, P., Petta, J. R. & Nakamura, Y. Hybrid quantum systems with circuit quantum electrodynamics. *Nat. Phys.* **16**, 257–267 (2020).
4. Suleymanzade, A. et al. A tunable high-q millimeter wave cavity for hybrid circuit and cavity qed experiments. *Appl. Phys. Lett.* **116**, 104001 (2020).
5. Kimble, H. J. The quantum internet. *Nature* **453**, 1023–1030 (2008).
6. Lauk, N. et al. Perspectives on quantum transduction. *Quantum Sci. Technol.* **5**, 020501 (2020).
7. Davis, E., Bentsen, G. & Schleier-Smith, M. Approaching the Heisenberg limit without single-particle detection. *Phys. Rev. Lett.* **116**, 053601 (2016).
8. Swingle, B., Bentsen, G., Schleier-Smith, M. & Hayden, P. Measuring the scrambling of quantum information. *Phys. Rev. A* **94**, 040302 (2016).
9. Daley, A. J. et al. Practical quantum advantage in quantum simulation. *Nature* **607**, 667–676 (2022).
10. Arute, F. et al. Quantum supremacy using a programmable superconducting processor. *Nature* **574**, 505–510 (2019).
11. Diamanti, E., Lo, H.-K., Qi, B. & Yuan, Z. Practical challenges in quantum key distribution. *npj Quantum Inf.* **2**, 16025 (2016).
12. Briegel, H.-J., Dür, W., Cirac, J. I. & Zoller, P. Quantum repeaters: the role of imperfect local operations in quantum communication. *Phys. Rev. Lett.* **81**, 5932–5935 (1998).

13. Svensson, K. et al. Figures of merit for quantum transducers. *Quantum Sci. Technol.* **5**, 034009 (2020).
14. McKenna, T. P. et al. Cryogenic microwave-to-optical conversion using a triply resonant lithium-niobate-onsapphire transducer. *Optica* **7**, 1737–1745 (2020).
15. Xu, Y. et al. Bidirectional interconversion of microwave and light with thin-film lithium niobate. *Nat. Commun.* **12**, 4453 (2021).
16. Sahu, R. et al. Quantum-enabled operation of a microwave-optical interface. *Nat. Commun.* **13**, 1276 (2022).
17. Andrews, R. W. et al. Bidirectional and efficient conversion between microwave and optical light. *Nat. Phys.* **10**, 321–326 (2014).
18. Brubaker, B. M. et al. Optomechanical ground-state cooling in a continuous and efficient electro-optic transducer. *Phys. Rev. X* **12**, 021062 (2022).
19. Delaney, R. D. et al. Superconducting-qubit readout via low-backaction electro-optic transduction. *Nature* **606**, 489–493 (2022).
20. Mirhosseini, M., Sipahigil, A., Kalaee, M. & Painter, O. Superconducting qubit to optical photon transduction. *Nature* **588**, 599–603 (2020).
21. Forsch, M. et al. Microwave-to-optics conversion using a mechanical oscillator in its quantum ground state. *Nat. Phys.* **16**, 69–74 (2020).
22. Barends, R. et al. Minimizing quasiparticle generation from stray infrared light in superconducting quantum circuits. *Appl. Phys. Lett.* **99**, 113507 (2011).
23. Covey, J. P., Sipahigil, A. & Saffman, M. Microwave-to-optical conversion via four-wave mixing in a cold ytterbium ensemble. *Phys. Rev. A* **100**, 012307 (2019).
24. Petrosyan, D., Mølmer, K., Fortágh, J. & Saffman, M. Microwave to optical conversion with atoms on a superconducting chip. *New J. Phys.* **21**, 073033 (2019).
25. Hafezi, M. et al. Atomic interface between microwave and optical photons. *Phys. Rev. A* **85**, 020302 (2012).
26. Vogt, T. et al. Efficient microwave-to-optical conversion using Rydberg atoms. *Phys. Rev. A* **99**, 023832 (2019).
27. Tu, H.-T. et al. High-efficiency coherent microwave-tooptics conversion via off-resonant scattering. *Nat. Photon.* **16**, 291–296 (2022).
28. Hermann-Avigliano, C. et al. Long coherence times for Rydberg qubits on a superconducting atom chip. *Phys. Rev. A* **90**, 040502 (2014).
29. Mohapatra, A. K., Jackson, T. R. & Adams, C. S. Coherent optical detection of highly excited Rydberg states using electromagnetically induced transparency. *Phys. Rev. Lett.* **98**, 113003 (2007).
30. Ningyuan, J. et al. Observation and characterization of cavity Rydberg polaritons. *Phys. Rev. A* **93**, 041802 (2016).
31. Jia, N. et al. A strongly interacting polaritonic quantum dot. *Nat. Phys.* **14**, 550–554 (2018).
32. Georgakopoulos, A., Sommer, A. & Simon, J. Theory of interacting cavity Rydberg polaritons. *Quantum Sci. Technol.* **4**, 014005 (2018).
33. Leroux, I. D., Schleier-Smith, M. H. & Vuletíc, V. Implementation of cavity squeezing of a collective atomic spin. *Phys. Rev. Lett.* **104**, 073602 (2010).
34. Anferov, A., Suleymanzade, A., Oriani, A., Simon, J. & Schuster, D. I. Millimeter-wave four-wave mixing via kinetic inductance for quantum devices. *Phys. Rev. Appl.* **13**, 024056 (2020).
35. Pechal, M. & Safavi-Naeini, A. H. Millimeter-wave interconnects for microwave-frequency quantum machines. *Phys. Rev. A* **96**, 042305 (2017).
36. Dixit, A. V. et al. Searching for dark matter with a superconducting qubit. *Phys. Rev. Lett.* **126**, 141302 (2021).
37. Khabiboulline, E. T., Borregaard, J., De Greve, K. & Lukin, M. D. Optical interferometry with quantum networks. *Phys. Rev. Lett.* **123**, 070504 (2019).
38. Groszkowski, P., Koppenhöfer, M., Lau, H.-K. & Clerk, A. A. Reservoir-engineered spin squeezing: macroscopic even-odd effects and hybrid-systems implementations. *Phys. Rev. X* **12**, 011015 (2022).
39. Cohen, L. Z., Kim, I. H., Bartlett, S. D. & Brown, B. J. Low-overhead fault-tolerant quantum computing using long-range connectivity. *Sci. Adv.* **8**, eabn1717 (2022).
40. Endres, M. et al. Atom-by-atom assembly of defect-free one-dimensional cold atom arrays. *Science* **354**, 1024–1027 (2016).
41. Welte, S., Hacker, B., Daiss, S., Ritter, S. & Rempe, G. Photon-mediated quantum gate between two neutral atoms in an optical cavity. *Phys. Rev.* **8**, 011018 (2018).

Article

Methods

Transduction scheme

Our transduction scheme is schematically outlined in Fig. 1a. For the case of mmwave-to-optical conversion, the atoms are first off-resonantly coupled from the ground $|g\rangle$ ($5S_{1/2}$) to the $|f\rangle$ ($35P_{1/2}$) Rydberg state by a 297 nm UV laser. Due to detuning, the atomic ensemble can resonantly and collectively absorb a 297 nm UV photon only if it then also absorbs a signal mmwave photon (occupying mode b), producing a collective excitation in the $|r\rangle$ ($36S_{1/2}$) state. The excited atom is then stimulated to emit a 481 nm blue photon, de-exciting it to the $|e\rangle$ ($5P_{3/2}$) state, and finally to spontaneously emit a 780 nm signal photon into the optical cavity mode a, closing the loop back to the initial ground state and completing the transduction process. For the cavity emission to be collectively enhanced, the loop must be closed to the same many-particle quantum state (ignoring atomic decay into free space), including all atomic motional and internal degrees of freedom. This can also be understood as requiring that no information about the fields be left behind in the state of the atoms, which would destroy the interference that produces collective enhancement. This enforces stringent phase- and mode-matching constraints that we satisfy by co-aligning the optical cavity mode with the 481 nm and UV control fields (see below and Supplementary Information C). To avoid further complications from the magnetic substructure of the atoms, we optically pump them along the transport lattice direction in the presence of a large Zeeman field that splits the levels, and choose the polarizations of the optical fields such that the loop is deterministically closed (see below).

Experimental sequence

Our experiments take place in the cryogenic vacuum chamber shown in Extended Data Fig. 1c. They begin with a magneto-optical trap (MOT) of laser-cooled ^{85}Rb atoms loaded from a Rb dispenser. The dispenser is contained in a box at room temperature (Extended Data Fig. 1a and Supplementary Information A) to enable the atoms to thermalize to 300 K from their emission temperature of 750 K. The thermalized atoms leak through a hole in the MOT grating into the trapping region, where they are cooled and trapped at the zero of a quadrupole field, using lasers on the Rb D_2 line at 780 nm. ^{85}Rb is chosen, rather than the more typical ^{87}Rb, because of its higher isotopic abundance.

The MOT is loaded into a 785 nm transport lattice via polarization gradient cooling to 5 µK (Supplementary Information A). The atoms are then transported from the MOT region into the crossed optical and mmwave cavity science region, in 14 ms, by smooth detuning of one of the lattice beams using a radio frequency system-on-chip (RFSoC)-based scriptable direct digital synthesizer (DDS) based on custom firmware that drives double-passed acousto-optic modulators (AOMs).

Once the atoms are in the science region, we optically pump them along the transport lattice direction in the presence of a large Zeeman field that splits the levels, and choose the polarizations of the optical fields such that the interconversion loop is deterministically closed (see below). Specifically, the atoms are pumped into the $|F_g = 3, m_F = 3\rangle$ state, using σ^+ polarized light on the the $F_g = 3 \leftrightarrow F_e = 3$ transition of the D2 line. A magnetic field (about 3.2 G) was previously 'trapped' in the superconducting cavity along the lattice direction (Supplementary Information C). We then reduce the lattice depth to about 20%, or turn the lattice off entirely to avoid broadening of the dark polariton due to different light shifts for different atoms depending on their position in the lattice. A typical experiment involves observing the output of the optical cavity on one of the ports while (1) probing with 780 nm light on the other port, (2) operating the transducer or (3) both, as in Fig. 3c. In experiments involving the UV beam we limit the cumulative 'on time' of the UV beam to below 300 µs per shot. This is done to avoid optical damage to the mirror coating from UV exposure. When external mmwave drives are required (either as signal photons for conversion or for off-resonantly tuning the atomic transition), we turn them on when the atom transport is initiated. The transduction process is controlled by turning on or off the 481 nm and UV beams. For experiments in Fig. 3a,b, each shot typically involved five 10-µs-long transduction steps separated by 50 µs of optical pumping. Optical pumping is required because the transduction process leads to depolarization of atoms, primarily due to decay of the atomic population from the $5P_{3/2}$ state, because our optical cavity is not on a cycling transition (see below and Extended Data Fig. 2). This effect, which leads to reduction in efficiency from the reduced optical cooperativity and reabsorption outside the four-level model that we employ throughout the manuscript, is separate from the optical–cooperativity scaling limit resulting from decay of collective excitations discussed elsewhere in the manuscript. The rate of this depumping depends on the mmwave drive strength and repeated optical pumping is not always necessary, as in the case of measuring correlations of thermal photons in Fig. 4, which involved simply a single 200-µs-long transduction step in each shot. All optical signals are collected with two single-mode, fibre-coupled, single-photon counting modules (SPCM, Excelitas SPCM AQRH-14-FC) after a non-polarizing beam splitter; the transistor–transistor logic (TTL) pulses generated by the individual photon arrivals are time tagged at a resolution of around 10 ns and stored for later analysis, using custom firmware in a field-programmable gate array (FPGA).

Directly driving and probing the mmwave cavity is achieved with the 100 GHz circuit shown schematically in Extended Data Fig. 1b. The 'science' mode of the cavity is at approximately 99.424 GHz and the 'tuning' mode at approximately 101.318 GHz. For transduction experiments, the science mode power is actively stablized by diverting most of it to a Mi-wave 950W/387 mmwave power detector and feedback to a Mi-wave 900WF-30/388 voltage-controlled attenuator.

Polarizations, trapping permanent magnetic field and optical pumping

The detailed-level scheme and various light polarizations for our experiment are shown in Extended Data Fig. 2a. The mmwave resonator was designed and tuned such that the science mode is polarized along the optical cavity axis. Whereas this was chosen, in part, to simplify couplings when atoms are optically pumped along the optical cavity axis (for experiments exploring non-linear physics), it turned out to be detrimental for transduction. For experiments in this paper, optical pumping and therefore the quantization axis are chosen to lie along the transport lattice direction. Two main constraints dictated by transduction led to this choice. The first constraint is phase matching of the transduction fields (Supplementary Information B and D), which demands that the **k** vectors of the absorbed (emitted) UV and mmwave fields be equal to the **k** vectors of the emitted (absorbed) probe and

$$\mathbf{k_{UV}} + \mathbf{k_{mm}} = \mathbf{k_{probe}} + \mathbf{k_{481}} \tag{3}$$

Because $1/|\mathbf{k_{mm}}|$ is much larger than the size of the atom effects of the phase, variation of the mmwave mode can be neglected. Thus the phase-matching condition requires that the 481 nm and UV laser beams have the same propagation direction as the cavity probe. The second constraint is that the net polarization change along the conversion loop should be 0, such that the loop begins and ends in the same atomic total angular momentum state.

The level scheme and polarizations shown in Extended Data Fig. 2a are among the ways used to satisfy these constraints, along with the limitation that the mmwave mode is polarized along the optical cavity axis. The 780 nm probe (or interconverted 780 nm photons) and the 481 nm are π polarized. Whereas sending in pure σ^- polarized UV field would have been ideal for Ω_{uv}, the phase-matching constraint restricts us to send in linearly polarized light out of which the σ^- component couples to the ground-state $5S_{1/2} \leftrightarrow 35P_{1/2}$ transition and σ^+ does not couple to the ground state at all. Similarly, whereas the mmwave cavity field is linearly polarized for this choice of quantization axis, only the σ^+ component couples to the $35P_{1/2}, m_j = -1/2$ state.

The superconducting Nb spacer shields the location of atoms at the intersection of the waveguides from any externally applied in magnetic fields not applied before cool-down. To impose the optimum magnetic fields for optical pumping, the spacer is heated to about 10 K (above the superconducting temperature of Nb at around 9.2 K) using a heating resistor thermally shorted to the spacer. At 10 K, because applied B-fields are not repelled by the Meissner effect, we optimize optical pumping beam polarization and the required magnetic fields by measuring depumping to the $F = 2$ state from the optical pumping beam (without a repump) through vacuum Rabi splitting (VRS) of optical cavity transmission. One subtle point is that we have to wait about 300 ms for the fields to settle after applying them, due to Eddy currents. This is necessary because the subsequent trapping of the fields is done in steady state. Once the correct fields are determined, we hold them and cool the spacer to 5 K. This traps a permanent field inside the cylindrical waveguides due to the appearance of persistent currents—a combination of Lenz's law and the Meissner effect[42].

Because these fields will stay frozen inside the cavity throughout, they also Zeeman-shift the $35P_{1/2}$ and $36S_{1/2}$ levels during probing. The choice of the magnitude and sign of the frozen field is dictated by the desired detuning between the $35P_{1/2} \leftrightarrow 36S_{1/2}$ mmwave transition and the mmwave cavity—it should be in a range such that ac-Stark shifts from classical fields applied to the tuning mode of the mmwave cavity can shift the atoms to resonance with the science mode, but far enough so as to not induce Purcell broadening without tuning. For this experiment, the field was chosen such that the transition was approximately 12.4 MHz detuned from the mmwave cavity.

Stark tuning the mmwave transition
We coarse-tuned the mmwave cavity close to the atomic transition using a combination of etching and mechanical squeezing, resulting in a cavity transition frequency of 99.42376 GHz, roughly 6 MHz from atomic transition without a magnetic field (Supplementary Information A2). Whereas in principle it is possible to use magnetic fields to bridge this gap, it is desirable to have more 'real-time' control (which does not require retrapping fields) over this detuning to thoroughly explore the parameter space.

We achieve this by generating a mmwave Stark shift for both the $36S_{1/2}$ and $35P_{1/2}$ states using the field of the tuning mode at 101.318 GHz, as shown in Supplement Fig. 1 and Extended Data Fig. 3. In practice, we vary the tuning mmwave field power and measure the stark shift of the EIT line (and thus the $36S_{1/2}$ state). We use the calibration shown in Extended Data Fig. 3b to extract the $35P_{1/2}$ state shift, and thus the atomic resonance frequency shift. We precisely diagonalize a Hamiltonian containing all magnetic sublevels of the 36S, 35P and 35S manifolds and find the calculation to be in excellent agreement for the observed relative shifts of our $36S_{1/2}$ and $35P_{1/2}$ states.

Purcell-like broadening and the non-linear Hamiltonian
Without the UV beam, our system is described by the non-linear Hamiltonian (Supplementary Information B):

$$H = \delta_a a^\dagger a + \delta_b b^\dagger b + \delta_e E^\dagger E + \delta_r R^\dagger R + \Delta F^\dagger F + (g_{opt}\sqrt{N}\, aE^\dagger + \text{h.c.})$$
$$+ (\Omega_b E R^\dagger + \text{h.c.}) + (g_{mm} b^\dagger F^\dagger R + \text{h.c.}) \qquad (4)$$

where, in addition to the collective operators defined in the main text, we have introduced a new operator, $F^\dagger$, which creates a collective excitation in the $35P_{1/2}$ state. The last term in the Hamiltonian M2 captures the exchange of a collective excitation between the $35P_{1/2}$ and $35S_{1/2}$ states through the absorption or emission of a mmwave photon. It describes a Jaynes–Cummings-like coupling that makes the dynamics non-linear. Although this non-linearity is quite weak in our system due to the large mmwave cavity linewidth (resulting in a single-particle cooperativity of

around unity), we can observe its signature in the Purcell-like broadening of the data in Fig. 2c.

As described below, we employ this model to calibrate dispersive shifts of the dark polariton/EIT line to the coherently driven photon number in the cavity (n_{ph}) and show that a naive calculation based on lowest-order Stark shift would lead to significant overestimation of conversion efficiency. To explore the validity of the model, we numerically solve the master equation for this Hamiltonian with most parameters independently measured by fitting EIT and VRS spectra at a large detuning ($\Delta = 2\pi \times 12.4$ MHz), where non-linearity is inconsequential. We calculated (see below) g_{mm} and the number of thermal photons from first principles. The results are shown in Extended Data Fig. 4 and we find good agreement between data and model.

Relevant parameters for transduction
Extended Data Table 1 summarizes all experimentally measured or theoretically calculated parameters for our system. The key parameters that affect transduction are those that determine the three cooperativites mentioned in the main text and the following Methods section.

On the optical transition, we measure κ_{opt} by probing the transmission of the bare optical cavity and fitting it to a Lorentzian (Fig. 1c). We calculate the single atom–optical cavity coupling, g_{opt} from the known length of the optical cavity, the radii of curvature of the cavity mirrors and dipole matrix element for the $|5S_{1/2}, F = 3, m_F = 3\rangle \leftrightarrow |5P_{3/2}, F = 4, m_F\,3\rangle$ atomic transition[43]. Knowing g_{opt}, the effective atom number N can be deduced by measuring the VRS, $2g_{opt}\sqrt{N}$, from the transmission spectrum of the optical cavity without the 481 nm and UV beams. For the 481 nm transition, we measure the Rabi frequency, Ω_b and the decoherence rate of the collective $36S_{1/2}$ Rydberg state, Γ_R by fitting the EIT spectrum to analytical results from non-Hermitian perturbation theory. These methods have been previously detailed in ref. [31]. We note that whereas our atom cloud temperature of 4 μK suggests a Doppler decoherence rate of $2\pi \times 150$ kHz, the presence of the 481 nm beam suppresses this decoherence[32].

On the mmwave side, calculation of the single atom–mmwave cavity coupling, g_{mm}, requires knowledge of the electric field profile in the mmwave cavity mode and the dipole matrix element of the $|35P_{1/2}, m_J = -1/2\rangle \leftrightarrow |36S_{1/2}, m_J = 1/2\rangle$ transition. We simulate the electric field profile using the finite element method (in the software package Ansys HFSS). The dipole matrix element for atomic transition is calculated using the atomic Rydberg calculator python package[44]. We typically determine κ_{mm} from the reflection spectrum of the mmwave cavity using the circuit shown in Extended Data Fig. 1. We can also measure it 'in situ' using the atoms when they are far detuned ($2\pi \times 12.4$ MHz) from the cavity, by scanning mmwave drive frequency across the cavity resonance and plotting the ac-Stark shift of the dark polariton (Extended Data Fig. 2c). We find the two values to be in good agreement, showing that the presence of the high-powered 481 nm laser does not significantly affect mmwave cavity.

We note here that the decoherence rate of the $35P_{1/2}$ state, Γ_F, is inconsequential for the transduction process in our operation regime. This is true providing $|\Delta| \gg \Gamma_F/2$, where $|\Delta|$ is the magnitude of detuning between the atoms and the mmwave cavity, or equivalently, between the atoms and UV beam in the case of resonant operation. This can be understood in the following way: the UV beam drives atoms into a coherent spin state at a rate set by Δ and, providing this is much faster than Γ_F (which for us is set by Doppler broadening), coherence is continuously refreshed.

Conversion efficiency and cooperativities
Assuming single-ended cavities ($\kappa_j^{ext} = \kappa_j$), the conversion efficiency of the idealized optical ↔ mmwave interconverter reduces to (Supplementary Information B) $\eta_{o\leftrightarrow mm} = \frac{4C_o C_b C_{mm}}{(C_b + (1+C_{mm})(1+C_o))^2}$, where $C_o = N_g \frac{4g_{opt}^2}{\kappa_{opt}\Gamma}$ is collectively enhanced optical cooperativity, $C_{mm} = N_{mm} \frac{4g_{mm}^2}{\kappa_{mm}\gamma_r}$ is collectively enhanced mmwave cooperativity and $C_b = \frac{4\Omega_b^2}{\Gamma\gamma_r}$ is a generalized

cooperativity defined for the 481 nm EIT-control field. Here the number of effective ground-state atoms in the presence of UV dressing is $N_g = N\cos^2\theta$, whereas the number of effective atoms in the Rydberg P state is $N_{mm} = N\sin^2\theta$ where N is the total atom number and $\tan\theta = \left|\frac{\Omega_{uv}}{\Delta}\right|$ controls the dressing fraction of the relevant UV-dressed ground state.

Conversion efficiency is optimized by ensuring good impedance matching in the coupling between optical and mmwave channels (Supplementary Information B). At fixed C_o and C_{mm}, $\eta_{o\leftrightarrow mm}$ may thus be maximized by varying C_b (by changing Ω_b), yielding $C_b = (1 + C_o)(1 + C_{mm})$, with $\eta_{max} = \frac{C_o C_{mm}}{(1 + C_o)(1 + C_{mm})}$. It is apparent that η_{max} is then limited by the smaller of the two cooperativities. Our ability to divide the collective enhancement between optical and mmwave transitions via the UV dressing fraction thus strongly relaxes the performance requirements of both resonators. In practice we are often limited by 481 nm power, in which case we use the maximum available 481 nm power and achieve impedance matching by varying C_{mm} or C_o via the detuning (Δ) and atom number, and yielding $\eta_{max} \approx 1 - \frac{2}{\sqrt{C_b}}$ (Supplementary Information B). Whereas this simple scheme is most accurate for a running-wave 780 nm cavity, residual effects from the non-phase-matched running wave in our standing-wave cavity are suppressed by high cooperativity (Supplementary Information B); all theory curves reflect a full standing-wave model.

Measurement of internal conversion efficiency

We measure $\eta_{o\leftrightarrow mm}$, the internal conversion efficiency, by driving the mmwave cavity and measuring photon count rate at the output of one of the ports of the optical cavity. It can be shown (Supplementary Information B) that $\eta_{o\leftrightarrow mm} = \frac{1}{f_o}\frac{\kappa_{opt}}{\kappa_{opt}^{ext}}\frac{4(R - R_{th})}{\kappa_{mm}^{ext} n_{ph}}$, where R is the count rate measured at the SPCMs with a coherent drive, R_{th} is the background rate—primarily set by the interconversion of thermal mmwave photons, f_o is the efficiency of the optical path outside the optical cavity—including the photon detection efficiency of the SPCMs, κ_{opt}^{ext} is the outcoupling rate of the relevant port of the optical cavity and n_{ph} is the expected photon occupation of just the bare mmwave cavity for a given coherent drive strength (minus the thermal occupation). We measure the efficiency of the optical path excluding the SPCM efficiency at approximately 0.5 and, independently, the efficiency of the SPCMs at approximately 0.56(5). We measure $\frac{\kappa_{opt}^{ext}}{\kappa_{opt}} = 0.63$ by reflection spectroscopy on the relevant optical port (Extended Data Fig. 2b). This measurement, as well as the optical cavity linewidth, is in line with the measured mirror reflectivities from the manufacturer (Layertec).

We calibrate n_{ph} by probing dark polariton resonance weakly (in the absence of UV) and measuring its shift as the mmwave cavity is driven in the dispersive limit (Extended Data Fig. 5a), $\Delta = 2\pi \times 1.4$ MHz $\gg g_{mm} = 2\pi \times 180$ kHz. To the lowest order in perturbation theory, the shift of the EIT peak is $\approx \frac{n_{ph}g_{mm}^2 \sin^2(\theta_D)}{\Delta}$, where $\theta_D = \tan^{-1}\left|\frac{Ng_{opt}}{\Omega_b}\right|$ is the dark-state rotation angle. Intuitively, this is just the lowest-order Stark shift of the atomic component of the dark polariton. By comparison with master equation simulations of the non-linear Hamiltonian M2, we actually find that this expression underestimates photon occupation and overestimates conversion efficiency by about 15%; going to one order higher in perturbation theory yields a modified analytical expression that matches well with the master equation prediction (Extended Data Fig. 5b and Supplementary Information C). We therefore use the modified expression to calibrate n_{ph}; the lowest n_{ph} we typically calibrate with this method is about 2 photons. Whereas we can resolve the smaller shifts induced by weaker drives, to avoid the effect of systematic fluctuations and to acquire a much stronger signal we calibrate weaker drives (as in Fig. 4) by, instead, measuring the count rate of interconverted photons and comparing this with the count rate of a dark polariton-shift-calibrated stronger drive. This assumes linearity of the transduction process, but both our measurements and mean-field simulations indicate that, for several photon drives, the process is comfortably within the linear regime.

Calculation of optical photon count rates and correlation functions

For the linearized system, it can be shown that

$$a_{out}(\omega) = S(\omega)b_{in}(\omega) \tag{5}$$

where $a_{out}(\omega)$ is the output optical field, $b_{in}(\omega)$ is the mmwave input field and $S(\omega)$ is the transfer function of the transducer between the external coupling port of the mmwave cavity and the measurement port of the optical cavity. The details for calculation of $S(\omega)$ for our system are covered in Supplementary Information B. We are interested in correlation functions of the form

$$g^{(1)}(\tau) = \langle a_{out}^\dagger(t + \tau)a_{out}(t)\rangle \tag{6}$$

The rate of the transduced optical photons at the output port of optical cavity is simply given by $g^{(1)}(0)$. It can be shown (Supplementary Information B) that, for a purely coherent input mmwave field of strength β, the first-order (field) correlator is given by

$$\bar{g}_{coh}^{(1)}(\tau) = \beta^2 |S(\omega_D)|^2 e^{-i\omega_D\tau} \tag{7}$$

where ω_D is detuning of the coherent drive from the mmwave cavity. For a thermal state input of n_{th} photons,

$$\bar{g}_{th}^{(1)}(\tau) = \frac{n_{th}}{2\pi}\int_{-\infty}^{\infty} |S(\omega)|^2 \kappa_{mm}^{ext} = \kappa_{mm}e^{-i\omega\tau}d\omega \tag{8}$$

For a coherently displaced thermal state, the rate at the output is just the sum of the individual coherent and thermal contributions. For the theory curves in Fig. 4, we calculate $g^{(1)}(0)$ and scale it by the experimentally measured loss in the optical path.

It can be further shown that, for a displaced thermal state, the second-order correlation function, $g^{(2)}(\tau) = \frac{\langle a^\dagger(t)a^\dagger(t+\tau)a(t+\tau)a(t)\rangle}{\langle a^\dagger(t)a(t)\rangle\langle a^\dagger(t+\tau)a(t+\tau)\rangle}$, is given by

$$g^{(2)}(\tau) = 1 + \frac{|\bar{g}_{th}^{(1)}(\tau) + \bar{g}_{coh}^{(1)}(\tau)|^2 - |\bar{g}_{coh}^{(1)}(\tau)|^2}{|\bar{g}_{th}^{(1)}(0) + \bar{g}_{coh}^{(1)}(0)|^2} \tag{9}$$

Note that in the absence of a coherent drive this reduces to the expected $1 + |g^{(1)}(\tau)|^2$, where $g^{(1)}(\tau)$ is now the normalized first-order correlation function.

Projected conversion efficiency with improvements

The main limitation to conversion efficiency is the 481 nm cooperativity, C_b, because the other cooperativities can be increased by increasing either the atom number or the Rydberg state dressing fraction by reducing detuning Δ. Some simple changes can significantly increase conversion efficiency. As stated above, the choice of Rydberg states and mmwave polarization, although first made for simplicity, is not ideal for transduction. Having a mmwave polarization orthogonal to the optical cavity axis would allow circular polarizations for all fields while maintaining phase matching. This would increase the 481 nm Rabi frequency, Ω_b, by a factor of 2. Raman sideband cooling of the atoms would allow us to significantly decrease the coherence decay rate of the collective $36S_{1/2}$ state, Γ_R, so that it is limited only by the decay of the Rydberg state. Cooling the atoms would also allow cloud compression by loading into an intracavity optical lattice or dipole trap, allowing us to significantly decrease the 481 nm beam size. We estimate that these improvements would allow 481 nm cooperativity to be

increased to about 2,400 from the current 30, leading to an efficiency of $1 - 2/\sqrt{C_b} \approx 0.96$. We also note that further increases are possible if a quasiphase-matching scheme is adapted (Supplementary Information D), which would allow implementation of a running-wave 481 nm optical cavity.

Overall conversion efficiency

The overall conversion efficiency is given by equation (2). For us, this is primarily limited by the low external coupling rate of the mmwaves, $\kappa_{mm}^{ext} = 2\pi \times 55$ kHz, which is more than a factor of 10 smaller than the overall κ_{mm}, set primarily by the internal losses of the mmwave cavity. This limits our overall conversion efficiency to approximately 2.5%. This κ_{mm}^{ext} is primarily a function of the length and diameter of the incoupling waveguide, but in our case the final value was obtained by adding a thin sheet of copper containing a small hole to reduce it even further (by a factor of 2). We chose this to minimize κ_{mm} and enable experiments that explore single-particle mmwave nonlinearity, in addition to experiments with quantum transduction. In fact, κ_{mm}^{ext} can be easily increased to 100-fold its current value by removal of the copper sheet and shortening the length of the incoupling waveguide by 2 mm. The corresponding decrease in mmwave cooperativity, C_{mm} can be compensated by increasing the $35P_{1/2}$ state dressing fraction. However, a more desirable regime for operation of the transducer would be lowering the temperature to 1 K, which would reduce the internal loss rate of the cavity to under $2\pi \times 10$ kHz[4]. At this point the external coupling can be increased by a factor of 10, resulting in roughly the same κ_{mm} and conversion bandwidth that we now have.

Data availability

Due to the proprietary format of the experimental data as collected for this manuscript, these are available from the corresponding author on request.

42. Meissner, W. & Ochsenfeld, R. A new effect when superconductivity occurs. *Science* **21**, 787–788 (1933).
43. Tanji-Suzuki, H. et al. Interaction between atomic ensembles and optical resonators: Classical description. In *Advances In Atomic, Molecular, and Optical Physics* (eds Arimondo, E. et al.) Vol. 60, 201–237 (Academic Press, 2011).
44. Sibalic, N., Pritchard, J., Adams, C. & Weatherill, K. ARC: an open-source library for calculating properties of alkali Rydberg atoms. *Comput. Phys. Commun.* **220**, 319–331 (2017).

Author contributions The experiments were designed by A.K., A.S., M.S., L.T., D.I.S. and J.S. The apparatus was built by A.K., A.S., M.S. and L.T. Collection of data was handled by A.K. and L.T. All authors analysed the data and contributed to the manuscript.

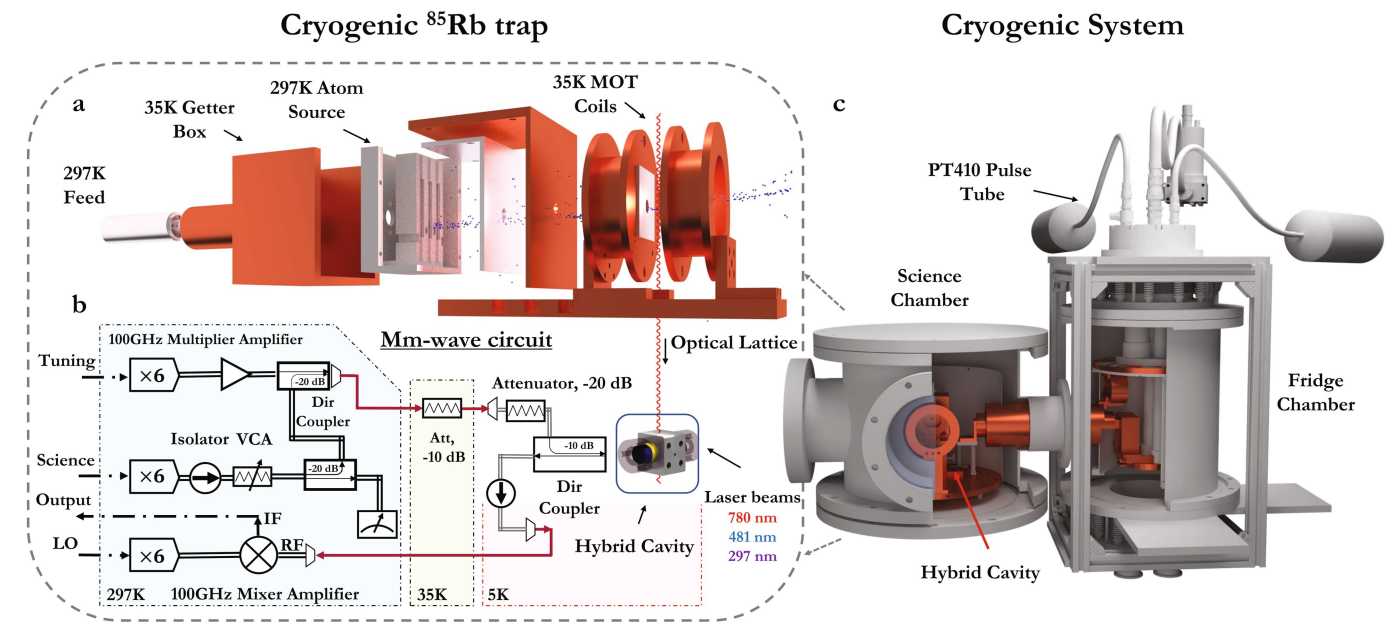**Competing interests** The authors declare no competing interests.

Extended Data Fig. 1 | Cryogenic System and mmwave control. a, Cryogenic ⁸⁵Rb trap. The atoms are emitted from a dispenser source mounted at room temperature, propagate through a small aperture at the back of the grating towards the capture volume of the grating MOT. The Helmholtz coils and all supporting structures are thermalized to 40K. **b**, Millimeter wave circuit used for characterizing the superconducting cavity and sending in mmwave photons for the interconversion experiment. Most of the power from the "science" source is diverted towards a power detector, which is used to actively stabilize the mmwave power using a voltage controlled attenuator (VCA). Both the science and the tuning sources are equipped with rf-switches to fully extinguish any signal to the cavity. **c**, The custom two-chambered 4K cryogenic system built for our hybrid cavity-QED experiments.

a

$|36S_{1/2}\ J = 1/2,\ m_J = 1/2\rangle$

π

$|35P_{1/2}\ J = 1/2,\ m_J = -1/2\rangle$

$|5P_{3/2}\ F = 4,\ m_F = 3\rangle$

π

$|5S_{1/2}\ F = 3,\ m_F = 3\rangle$

b

c
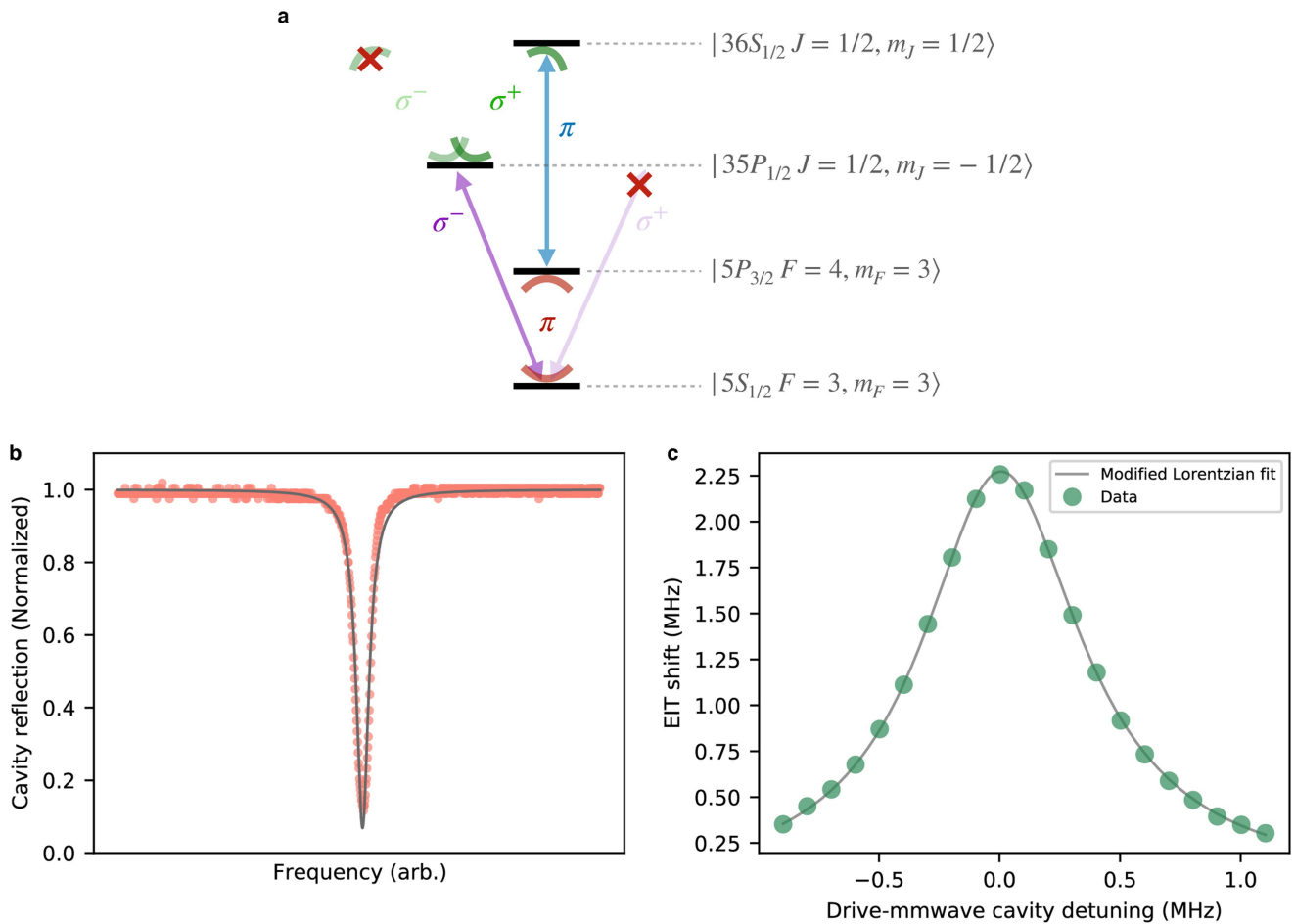
**Extended Data Fig. 2 | Level structure, polarizations, and cavity characterizations. a**, The levels and light polarizations involved in transduction. The mmwave cavity (green) science mode is linearly polarized along the optical cavity (red) direction. We choose (through a magnetic field and optical pumping) the quantization axis along the lattice beam direction to achieve phase matching and zero angular momentum change on a round trip at the same time. The mmwave mode polarization, which is orthogonal to this quantization axis, can be decomposed as a linear combination of σ^+ and σ^- polarizations. The UV beam (purple) is linearly polarized orthogonal to both the lattice direction and the optical cavity axis, and thus can also be decomposed as a linear combination of σ^+ and σ^- polarizations. The 481 nm beam and the 780 nm probe (or the emitted interconverted photon) are linearly polarized along the lattice direction, and therefore have π polarization with respect to the quantization axis. We start by optically pumping to the stretched hyperfine magnetic sublevel, which results in the UV σ^+ component and the

mmwave σ^- component not coupling to any available state. The effect of the Raman couplings generated from these polarizations is suppressed due to the magnetic field lifting the degeneracy. **b**, Reflection measurement off of the port of the optical cavity at which the photons are counted for any of our experiments described in the main text. The minimum reflection point directly yields $(1 - 2\kappa_{opt}^{ext}/\kappa_{opt})^2$. The gray line is a model fit, with slight deviations due to a small polarization splitting of the cavity, and polarization impurity of the probe. **c**, "In-situ" measurement of the mmwave cavity spectrum using the shift of the dark polariton/EIT resonance. The atomic transition is far-detuned ($2\pi \times 12.4$ MHz) from the cavity and a mmwave drive is scanned in frequency around the *cavity* resonance. The resulting ac-Stark shift of the dark polariton is porportional to the mmwave power in cavity. The gray line is a fit to a Lorentzian modified to account for the effect of the changing detuning of the drive from the atoms.

a

b
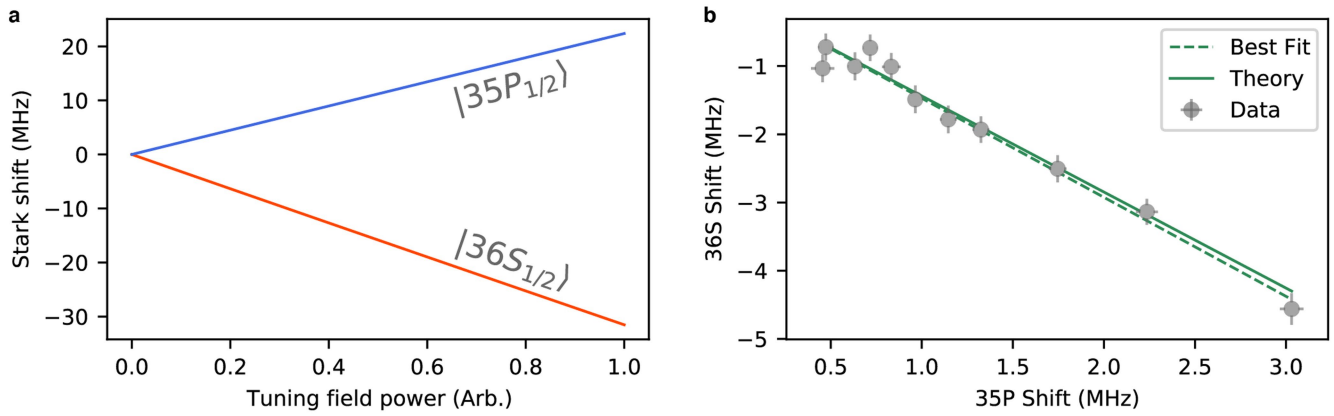
Extended Data Fig. 3 | Stark tuning of the atomic states. a, The calculated ac Stark shifts of the $36S_{1/2}$ and $35P_{1/2}$ "science" states as the power in the 101.318 GHz "tuning" mode of the cavity is increased. The tuning of the atomic states allows us to control the detuning (Δ) between the atomic transition and the mmwave cavity for transduction, as well as other experiments like those in Fig. 2c. **b**, As we vary the classical drive on tuning mode, we measure the shifts of the $36S_{1/2}$ and $35P_{1/2}$ states using a cavity Rydberg EIT and direct UV spectroscopy from the $5S_{1/2}$ state, respectively. This calibration then allows us to infer the $35P_{1/2}$ shift (which is more involved to measure day-to-day) from the $36S_{1/2}$ shift measured via cavity Rydberg EIT. We find excellent agreement between our calculation and the observed shifts.

a **b**
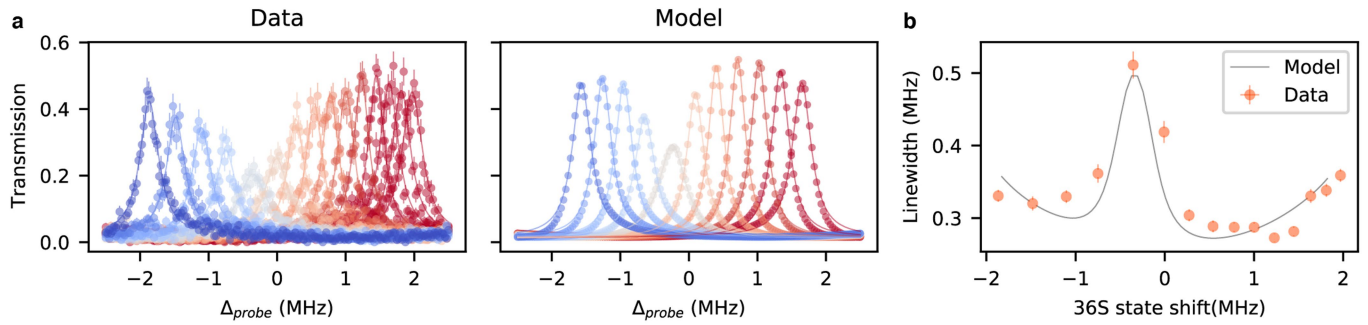
Extended Data Fig. 4 | Purcell-like broadening of the dark polariton. a, Same data as Fig. 2c, but the full data set with spectra at additional atom-mmwave cavity detunings (Δ in main text), which were omitted from the plot in the main text for clarity. For this dataset, we simply varied the strength of the "tuning" field to shift the atomic states, but did not change the 481 nm frequency – which would be required to keep the dark polariton at the same frequency as the optical cavity (at Δ_{probe} = 0 MHz). The asymmetry arises because at the point which the mmwave atomic transition is resonant with the mmwave cavity, the *optical cavity* and 481 nm beam are not resonant with the $5S_{1/2} \leftrightarrow 36S_{1/2}$ transition.

b, Master equation simulation of the data in **a**, using the non-linear Hamiltonian derived in SI B (equation S8), where all the parameters were experimentally measured using spectra with and without the 481 nm beam at a large Δ. This excludes g_{mm} and the number of thermal photons, which were calculated from first principles. In both **a** and **b**, the solid lines are Lorentzian fits. **c**, The linewidths obtained from the Lorentzian fits of both theory and experiment. We find excellent agreement between the two, building confidence in our model. The dark polariton starts to broaden again near the edges because of mixing with the bright polaritons.

Data

Theory
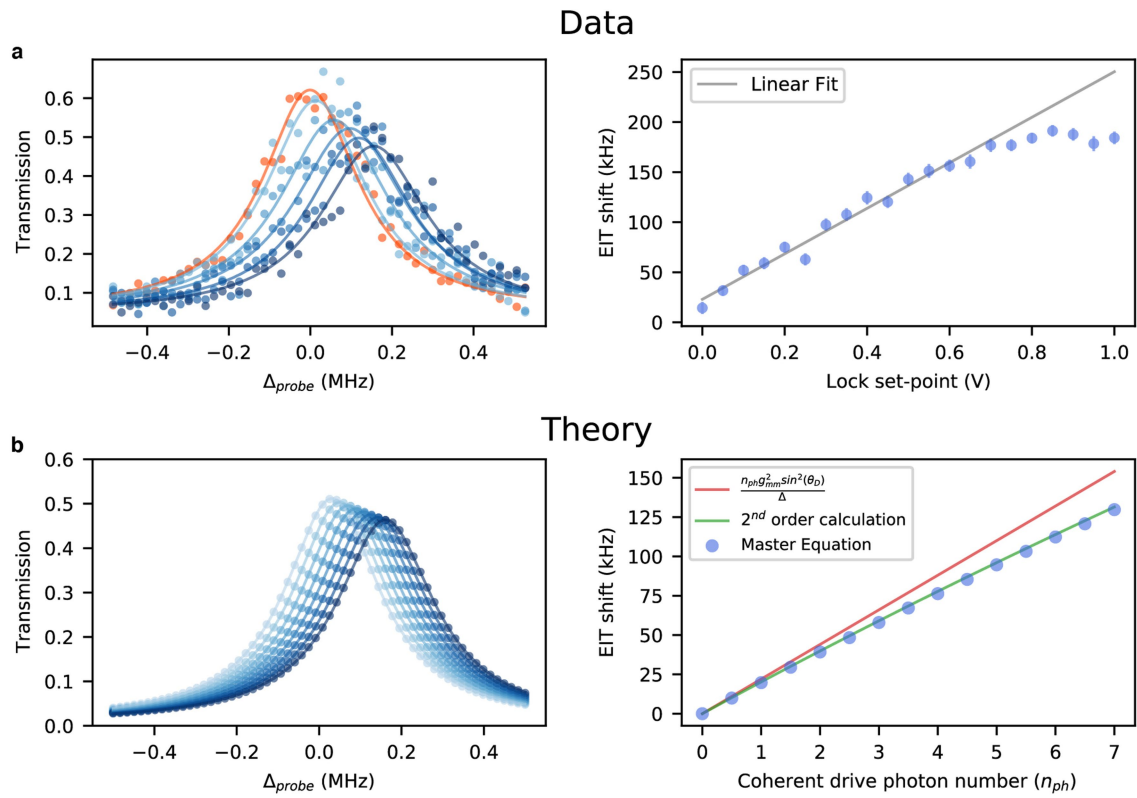
Extended Data Fig. 5 | Measuring intracavity photon number (n_{ph}) from dispersive shifts. a, Left - Measured dark polariton/Rydberg EIT spectra as the "science" mode drive strength is increased at an atom-mmwave cavity detuning, $\Delta = 2\pi \times 1.4$ MHz. We first measure a reference spectrum with the mmwave source entirely turned off using an rf-switch (orange). An actively locked mmwave drive (using a power detector and a VCA, see Methods A, Extended Data Fig. 1) is then applied with increasing strength (light blue to dark blue). The solid lines are Lorentzian fits. Right - The extracted shifts by fitting the spectra in the left panel as the lock set point is increased. Note that even at the lowest lock set-point, there is some leakage from the VCA, which necessitates measuring the orange reference in the left panel with no mmwave power from the source. After a threshold, the shifts saturate because the VCA reaches lowest attenuation and there is no more mmwave drive power available. **b**, Master equation calculation of the data in **a** using the non-linear Hamiltonian given by equation 4 with parameters independently measured or calculated from first principles (g_{mm} and number of thermal photons) and an added coherent drive. This calculation allows us to calibrate our coherently driven photon number (n_{ph}) and the dispersive shift of the EIT resonance. Left - The calculated spectra with Lorentzian fits. Right - The shift of the EIT resonance against the number of mmwave photons driven into the cavity by the coherent drive in steady state. The simple first order expression (red) over-estimates the shifts. We instead calculate and use a much more accurate analytical result (green) in SI C.

Extended Data Table 1 | Table of key experimental parameters

Parameter	Symbol	Value
Millimeter wave cavity "science" mode frequency	–	$2\pi \times 99.42376(1)$ GHz
Millimeter wave cavity "tuning" mode frequency	–	$2\pi \times 101.318$ GHz
$35P_{1/2} \leftrightarrow 36S_{1/2}$ transition frequency without stark tuning	–	$2\pi \times 99.436$ GHz
Single atom-optical cavity coupling	g_{opt}	$2\pi \times 206$ kHz
Optical cavity linewidth	κ_{opt}	$2\pi \times 1.71(4)$ MHz
Out-coupling rate of the measurement optical cavity port	κ_{opt}^{ext}	$2\pi \times 1.07(3)$ MHz
Decay rate of the $5P_{3/2}$ state	Γ	$2\pi \times 6.065$ MHz
481 nm beam Rabi frequency	Ω_b	$2\pi \times 1.45(5)$ MHz
Decoherence rate of the $36S_{1/2}$ collective state	Γ_R	$2\pi \times 56(8)$ kHz
Single atom-mmwave cavity coupling	g_{mm}	$2\pi \times 182$ kHz
Millimeter wave cavity linewidth	κ_{mm}	$2\pi \times 805(5)$ kHz
Millimeter wave cavity external coupling rate	κ_{mm}^{ext}	$2\pi \times 55(5)$ kHz
UV beam effective Rabi frequency	Ω_{UV}	$2\pi \times 230(3)$ kHz
Optical path efficiency including SPCM efficiency	f_o	$0.28(2)$